New observations of NGC 1624-2 reveal a complex magnetospheric structure and underlying surface magnetic geometry

David-Uraz, A.; Petit, V.; Shultz, M.E.; Fullerton, A.W.; Erba, C.; Keszthelyi, Z.; Seadrow, S.; Wade, G.A.

DOI
10.1093/mnras/staa3768

Publication date
2021

Document Version
Final published version

Published in
Monthly Notices of the Royal Astronomical Society

Citation for published version (APA):
David-Uraz, A., Petit, V., Shultz, M. E., Fullerton, A. W., Erba, C., Keszthelyi, Z., Seadrow, S., & Wade, G. A. (2021). New observations of NGC 1624-2 reveal a complex magnetospheric structure and underlying surface magnetic geometry. *Monthly Notices of the Royal Astronomical Society*, *501*(2), 2677-2687. https://doi.org/10.1093/mnras/staa3768

Monthly Notices
of the
ROYAL ASTRONOMICAL SOCIETY

MNRAS **501,** 2677–2687 (2021)
Advance Access publication 2020 December 14

doi:10.1093/mnras/staa3768

New observations of NGC 1624−2 reveal a complex magnetospheric structure and underlying surface magnetic geometry*

A. David-Uraz ,[1,2,3]† V. Petit ,[1,4] M. E. Shultz,[1] A. W. Fullerton,[5] C. Erba,[1] Z. Keszthelyi ,[6] S. Seadrow[1] and G. A. Wade[7]

[1] *Department of Physics and Astronomy, University of Delaware, Newark, DE 19716, USA*
[2] *Department of Physics and Astronomy, Howard University, Washington, DC 20059, USA*
[3] *Center for Research and Exploration in Space Science and Technology, and X-ray Astrophysics Laboratory, NASA/GSFC, Greenbelt, MD 20771, USA*
[4] *Bartol Research Institute, University of Delaware, Newark, DE 19716, USA*
[5] *Space Telescope Science Institute, Baltimore, MD 21218, USA*
[6] *Anton Pannekoek Institute for Astronomy, University of Amsterdam, Science Park 904, NL-1098 XH Amsterdam, the Netherlands*
[7] *Department of Physics and Space Science, Royal Military College of Canada, PO Box 17000, Stn Forces, Kingston, ON K7K 7B4, Canada*

Accepted 2020 December 1. Received 2020 December 1; in original form 2020 October 14

ABSTRACT

NGC 1624−2 is the most strongly magnetized O-type star known. Previous spectroscopic observations of this object in the ultraviolet provided evidence that it hosts a large and dense circumstellar magnetosphere. Follow-up observations obtained with the *Hubble Space Telescope* not only confirm that previous inference, but also suggest that NGC 1624−2's magnetosphere has a complex structure. Furthermore, an expanded spectropolarimetric time series shows a potential departure from a dipolar magnetic field geometry, which could mean that the strongest field detected at the surface of an O-type star is also topologically complex. This result raises important questions regarding the origin and evolution of magnetic fields in massive stars.

Key words: techniques: polarimetric – stars: early-type – stars: individual: NGC 1624−2 – stars: magnetic field – stars: winds, outflows – ultraviolet: stars.

1 INTRODUCTION

As sources of ionizing flux, momentum, and chemical enrichment, O stars represent formidable galactic engines, sculpting their immediate environment, and participating in the overall evolution of their galactic hosts (e.g. Chu 2003). Of particular interest is the subset (∼7 per cent; Grunhut et al. 2017) of O stars that exhibits a detectable surface magnetic field, thought to potentially be the progenitors of exotic objects and transients such as heavy stellar-mass black holes (Petit et al. 2017; Groh et al. 2020) and pair-instability supernovae (Georgy et al. 2017) even at solar metallicity, as well as magnetars (Ferrario & Wickramasinghe 2008).

There are many limitations to our understanding of these stars and of the role that they play in galactic ecology. The most obvious one concerns their rarity: only 11 such objects are known to exist so far (Petit et al. 2013; Fossati et al. 2016), making an in-depth characterization of their magnetic properties as a population difficult due to small number statistics. Furthermore, these stars have undergone 'magnetic braking' (Weber & Davis 1967; ud-Doula, Owocki & Townsend 2009) and hence are typically slow rotators, which means their detailed study requires long monitoring programs in some cases. Indeed, the O-type star with the longest known rotation period is the magnetic O4-8f?p star HD 108, with a period of ∼55 yr (Nazé et al. 2010; Shultz & Wade 2017). Even for those few stars that do have shorter rotation periods, other complications (such as binarity) muddle the interpretation of their observations and properties (e.g. HD 47129, also called 'Plaskett's star'; Grunhut et al. 2013).

That said, as far as we know from the results of large-scale spectropolarimetric surveys (e.g. Morel et al. 2015; Wade et al. 2016), magnetic O stars harbour essentially dipolar, globally organized fields on their surfaces, with strengths on the order of a few kG – with the notable exceptions of ζ Ori A and NGC 1624−2 on the lower (∼140 G; Blazère et al. 2015) and higher (∼20 kG; Wade et al. 2012) end of this range, respectively. Recent studies suggest that O stars might not follow the long-held assumption of magnetic flux conservation as they evolve (Landstreet et al. 2007, 2008; Fossati et al. 2016; Shultz et al. 2019; though large surveys may not as yet conclusively address this issue; Petit et al. 2019), although the details of the dissipation mechanism and rate remain unknown.

One key characteristic of magnetic O stars is the interplay between their dense, radiatively driven winds (e.g. Castor, Abbott & Klein 1975) and their magnetic fields, which channel and confine their outflows to form circumstellar *magnetospheres* (Landstreet & Borra 1978; Shore & Brown 1990; Babel & Montmerle 1997). Early magnetohydrodynamic (MHD) simulations provided valuable insights into the structure of magnetospheres, as well as their role in spinning down their host stars and inhibiting their gradual loss of mass throughout their main-sequence lifetimes (ud-Doula & Owocki 2002; ud-Doula, Owocki & Townsend 2008; ud-Doula et al. 2009).

---

* Based on observations made at the Canada-France-Hawaii Telescope (CFHT).

† E-mail: alexandre.daviduraz@howard.edu

Published by Oxford University Press on behalf of Royal Astronomical Society

Incorporation of these effects into dedicated evolutionary models has profound consequences on the end points of the evolution of magnetic massive stars (e.g. Meynet, Eggenberger & Maeder 2011; Keszthelyi et al. 2019, 2020).

Given that most magnetic O stars have very low rotation rates (as a consequence of the braking mentioned above; Petit et al. 2013), the confined wind material within their magnetospheres is not centrifugally supported and therefore the analytic prescription of Owocki et al. (2016) – or analytic dynamical magnetosphere (ADM) model – presents a practical time-averaged view of the structure of the magnetosphere that agrees well with earlier MHD investigations. Such a prescription is ideally suited to the interpretation of various multiwavelength magnetospheric diagnostics (such as Hα, Owocki et al. 2016; X-ray emission, Nazé et al. 2014; optical broad-band photometry, Munoz et al. 2020; as well as ultraviolet (UV) resonant line profiles, Erba et al. 2020), without the computational cost associated with full-scale MHD simulations. Indeed, while none of these diagnostics individually contain sufficient information to construct a fully model-independent view of the magnetosphere (such as e.g. a three-dimensional tomographic Doppler reconstruction of the magnetospheric structure), qualitative inferences can be made in light of simple analytic tools such as the ADM model.

In particular, wind-sensitive UV resonance lines have historically been coupled very successfully with spherically symmetric models to provide important insights into the mass-loss properties of the general population of O stars (e.g. Bouret et al. 2003). Their ability to probe the density and velocity structure of the extended atmospheres of these stars makes them particularly useful in that regard, and that usefulness carries over to magnetic stars as well, although the assumption of spherical symmetry breaks down and dedicated models must be used to interpret their variations. For instance, assuming a globally organized dipolar field, it is fairly simple to distinguish between different viewing angles. The general phenomenology of the UV line profile variations (e.g. Marcolino et al. 2013) can be framed in terms of the rotational phases associated with the 'high' ($\phi = 0.0$) and 'low' ($\phi = 0.5$) states, which are defined respectively by the maximum and minimum of the variation exhibited by the equivalent width of Hα. In the context of the oblique rotator model (Stibbs 1950), variations in the equivalent width of Hα are attributed to changes in the projected surface area of the region of enhanced magnetospheric emission that forms in the magnetic equatorial plane. Consequently, the 'high' state corresponds to times when the magnetic pole is most closely aligned to the observer's line of sight, while the 'low' state occurs when the magnetic equator is closest to being viewed edge on. Within that framework, 'strong' UV resonance lines (i.e. with large oscillator strengths, and thus nearly optically thick when formed in dense O-star winds) show enhanced high-velocity absorption at high state, since we are looking through wind material flowing nearly radially along open magnetic field lines, while enhanced absorption can be observed near line centre in both strong and weaker lines in the low state (e.g. Nazé et al. 2015).

The archetype of an O star magnetosphere can be found around the Of?p[1] star NGC 1624−2 (O7f?p; Walborn et al. 2010). Discovered to host the strongest known magnetic field at the surface of an O-type star by almost an order of magnitude (∼20 kG, assuming a dipolar geometry; Wade et al. 2012), it is also the only star of that peculiar spectral type to exhibit clearly separated Zeeman components in its integrated Stokes I line profiles. This allows for a complementary measure of the disc-integrated field modulus (in addition to the usual disc-integrated longitudinal field measurements enabled by circular polarization and typically used to diagnose magnetic fields in massive stars). Preliminary attempts (which we revisit in this paper with additional monitoring) to reconcile both field modulus and longitudinal field measurements have so far failed to do so using a solely dipolar field, hinting at a more complex magnetic geometry (Wade et al. 2012; MacInnis 2016; David-Uraz et al. 2017).

Previous X-ray and UV investigations have found NGC 1624−2 to be surrounded by a giant magnetosphere, as expected from its large Alfvén radius ($R_{\rm A}/R_* \sim 11.4$; Wade et al. 2012), the largest of any O-type star. Petit et al. (2015) showed that it must be large and dense, as it absorbs up to 95 per cent of the intrinsic circumstellar X-ray emission, a result further supported by David-Uraz et al. (2019), who found it to cause very large line profile variations in the UV.

In this paper, we present new UV spectra taken with the *Hubble Space Telescope* (*HST*) and spectropolarimetric observations taken at the Canada–France–Hawaii Telescope (CFHT) and the Télescope Bernard Lyot (TBL). In Section 2, we provide more details about the observations, while the UV and magnetic results are presented in Section 3. Finally, we interpret these results and offer our conclusions in Section 4.

2 OBSERVATIONS

2.1 Ultraviolet spectroscopy

Previous observations of NGC 1624−2 were obtained by General Observer (GO) Program 13734 (PI: Petit; David-Uraz et al. 2019) with the Cosmic Origins Spectrograph (COS) on-board the *Hubble Space Telescope* (*HST*), and sampled the morphology of the key UV resonance lines at the phases of the 157.99 d period associated with the 'high' ($\phi \sim 0.0$) and 'low' ($\phi \sim 0.5$) states. GO Program 15066 (PI: David-Uraz) also used COS to obtain four additional UV spectra of NGC 1624–2 near the two quadrature phases, in order to assess asymmetries in the structure of the magnetosphere. Table A1 summarizes the available UV spectroscopy of NGC 1624–2.

Each COS observation obtained by GO Program 15066 consisted of a two-orbit visit. For each visit, the first orbit began with a guide-star acquisition by the Fine Guidance Sensor (FGS) followed by a target acquisition using the imaging mode of COS with the near-UV channel, Mirror A, and the bright-object aperture (BOA). After the execution of a small-angle maneuver to centre NGC 1624–2 accurately in the primary science aperture (PSA; 2.5 arcsec diameter), spectra with the G130M grating centred on 1222 and 1291 Å were obtained. During the second orbit, exposures with the G160M grating centred on wavelengths of 1577 and 1623 Å were acquired. Both channels of the far-UV cross-delay (XDL) line detector were used to make the observations in time-tag mode.

These four instrumental configurations provided useful wavelength coverage from about 1150 to 1800 Å with a resolving power that increases linearly with wavelength from ∼16 000 to ∼21 000 over the respective ranges of both gratings. For each grating setting, the total exposure time indicated in Table A1 was divided into subexposures of equal duration but slightly different positions [fixed pattern positions (FP-POS)] on the detector to mitigate the effects of fixed-pattern noise in the combined 'x1dsum' spectrum. Since the observations were made at COS lifetime position 4, only two FP-POS positions were available for the G130M/1291 configuration. For all other configurations, four FP-POS positions were used.

The spectra were uniformly processed with version 3.3.4 (2018-01-08) of the CALCOS calibration pipeline. Calibration steps in-

---

[1] This spectral class was defined by Walborn (1972) and found to be related to magnetism by Grunhut et al. (2017).

cluded: correcting the photon-event table for dead-time and positional effects such as drifts in the detector electronics, geometric distortion, and the Doppler shift of the observatory; binning the time-tag data and assigning wavelengths to the bins on the basis of Pt–Ne spectra acquired simultaneously with spectra of NGC 1624–2; extraction and photometric calibration of 1D spectra; and the 'shift and add' combination of spectra taken at different FP-POS positions for each grating setting.

2.2 Optical spectropolarimetry

NGC 1624−2 was observed with the Echelle SpectroPolarimetric Device for the Observation of Stars (ESPaDOnS; Donati et al. 2006) at the CFHT, as part of observing programs 12AP14, 12BP13, and 13BC05 (PI: Wade), as well as program 15BC13 (PI: Petit). This instrument has a high resolving power ($R \sim 65\,000$) and covers a wavelength range of about 3600–10 000 Å. In total, 22 observations (including five that were previously analysed by Wade et al. 2012), each consisting of four subexposures, were obtained between 2012 and 2015. Data reduction was performed using the UPENA pipeline (Martioli, Teeple & Manset 2011) based on the LIBRE-ESPRIT reduction package (Donati et al. 1997). It combines the aforementioned subexposures (each corresponding to a different angle of the Fresnel rhombs) to yield integrated spectra (Stokes I parameter), as well as circularly polarized spectra (Stokes V parameter), which are sensitive to the Zeeman effect (e.g. Landi degl'Innocenti & Landolfi 2004), thus allowing us to detect and measure astrophysical magnetic fields. It also produces two diagnostic nulls (N), which characterize the level of noise and allow us to identify potential spurious signals in the Stokes V spectra.

We also included an additional observation obtained with NARVAL (a twin instrument) using the TBL (program L121N02), which was included in the analysis of Wade et al. (2012). These observations are detailed in Table A2, together with mean longitudinal field measurements, while separate longitudinal field measurements obtained from single lines (see Section 3.2) appear in Table A3.

3 RESULTS

3.1 UV analysis

The new spectra were continuum normalized. In particular, we focused on the profiles of the same wind-sensitive lines that were studied by David-Uraz et al. (2019), namely the Si IV λλ1393, 1402 and C IV λλ1548, 1550 doublets. These lines probe two important regimes of opacity, and in the context of a simple dipolar magnetic field, their variation can be understood in terms of the geometry (density and velocity) of the magnetospheric plasma. Indeed, building upon the picture presented in Section 1, the general phenomenology can be understood as follows: the unconfined wind material along the magnetic poles escapes nearly radially at high velocity and is rarefied, while around the magnetic equator, the dense magnetically confined material moves at a lower velocity, and mostly in the latitudinal direction (with respect to the magnetic axis). Therefore, a weaker line like the Si IV doublet probes mostly high-density regions near the stellar surface, leading to low-to-moderate velocity emission at high state, when the dense material trapped near the equator is seen off-limb, and to strong absorption near line centre (and *stronger* absorption generally) when that same material occults the star at low state. Additionally, a stronger line such as the C IV doublet is also sensitive to the rarefied near-terminal[2] wind streaming above the magnetic pole, which means that there should be additional high-velocity blueshifted absorption at high state. This picture corresponds to the general case described by Nazé et al. (2015), as well as what was observed by David-Uraz et al. (2019), who also pointed out that the Si IV and C IV line profiles in the spectra of NGC 1624−2 exhibit overall more emission than those of comparable non-magnetic stars (due to the overdense confined magnetic equatorial region, compared to a spherically symmetric wind) and much greater variability than even those of other magnetic O-type stars.

A comparison of the newly obtained profiles with those obtained previously by David-Uraz et al. (2019) is presented in Fig. 1. While one would normally expect to see – assuming that the magnetosphere is formed by a global dipolar field – a gradual transition (e.g. Erba et al. 2020) between the high- and the low-state profiles, and vice versa, that is not what is observed.

Instead, every newly observed line profile closely resembles one of the previous two observations. In particular, observations obtained at rotational phases ∼0.36 and ∼0.62 are very similar to the previous high-state observation obtained at phase ∼0.99, in that they present enhanced emission in the Si IV doublet and enhanced absorption at high velocities (i.e. in the blue vertical band in Fig. 1) on the blue side of the C IV doublet. Similarly, observations obtained at phases ∼0.27 and ∼0.87 are very similar to the previous low-state observation obtained at phase ∼0.45, with stronger absorption close to line centre in both doublets. In fact, the observation at phase 0.62 appears to exhibit even more extreme high-state line profile features than that at phase 0.99, with even stronger emission at low velocities in the Si IV doublet and deeper absorption at high velocities on the blue side of the C IV doublet.

In principle, one might have expected that either the high state and low state do not quite correspond to magnetic pole-on and equator-on views, respectively, or that the viewing angle crosses the magnetic equator more than once over the course of a rotational cycle, leading to double-wave variations of the line profile variability described above. That said, neither one of these scenarios can explain: (i) the fact that observations taken at *three* separate rotational phases show similar line morphologies, and (ii) that the 'high-state-like' and 'low-state-like' morphologies alternate throughout a rotational cycle. This is also at odds with the behaviour of other magnetospheric diagnostics, such as Hα emission (Wade et al. 2012).

To further illustrate this point, we compute equivalent widths using the wavelength ranges shown in Fig. 1: the full ranges of the Si IV doublet and of the absorption trough of the C IV doublet, as well

---

[2] Wade et al. (2012) report NGC 1624−2's terminal velocity to be 2875 km s^{-1}, based on a theoretical scaling (Lamers, Snow & Lindholm 1995) with its escape velocity. This represents, in principle, the terminal velocity that the star would have, with its other properties (mass, radius, and luminosity) unchanged, in the absence of a magnetic field. However, the interaction with the magnetic field at the base of the wind can modify its overall driving, as evidenced by the latitudinal dependence of the surface mass flux in MHD simulations of magnetic massive stars (Owocki & ud-Doula 2004). Moreover, these same simulations also show that the polar flow can reach velocities greater than the nominal terminal velocity, due to additional driving allowed by the faster-than-radial divergence of the flux tubes, leading to rarefied material and consequently to desaturation in the high-velocity absorption trough of strong wind lines. Therefore, while this reported value of the terminal velocity should only be used as an estimate, a more profound understanding of the kinematics of the wind can only be obtained by fitting the UV wind-sensitive line profiles of NGC 1624−2 with appropriate, non-spherically symmetric models (e.g. Erba et al. 2020).

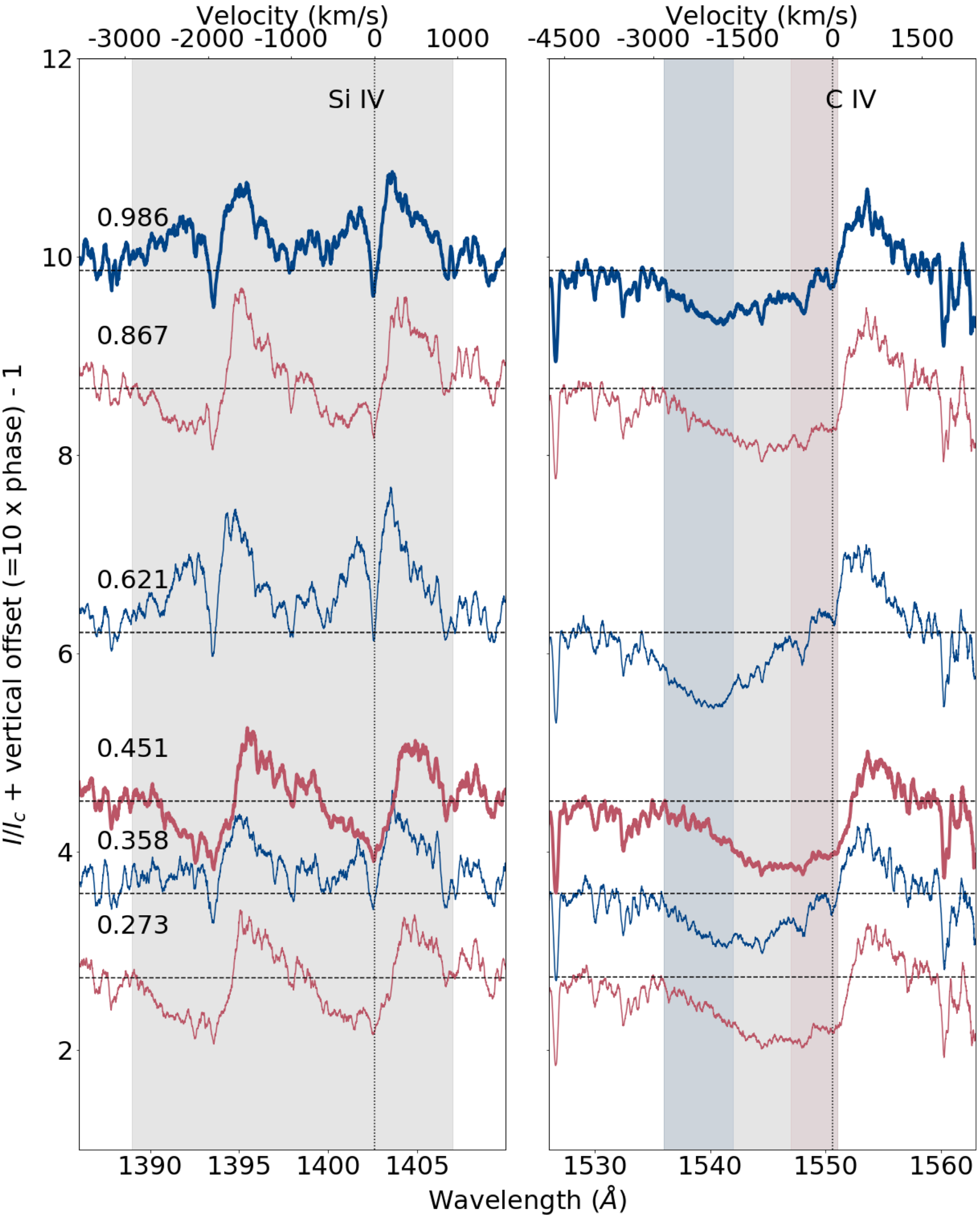

Figure 1. *HST*/COS spectra of NGC 1624−2 obtained at six different rotational phases, as computed using the ephemerides published by Wade et al. (2012). Each spectrum is vertically offset proportionally to its phase, which is included as a label. Magenta lines represent spectra that have 'low-state-like' behaviour, while blue lines represent 'high-state-like' spectra. The thicker lines correspond to spectra that were already presented by David-Uraz et al. (2019). These spectra were smoothed with a 21-pixel wide boxcar filter for display purposes. Vertical background bands correspond to ranges of integration for our equivalent width calculations, with the grey bands corresponding to the whole range of the Si IV doublet and of the absorption trough of the C IV doublet, and on the right, the overlaid magenta and blue bands correspond to the low- and high-velocity portions of the aforementioned absorption trough, which respectively characterize low-state-like and high-state-like morphological features. The top axis shows the corresponding velocities for each panel, in the reference frame of the star, with respect to the line centre of the red component of the doublet (indicated by a vertical dotted line).

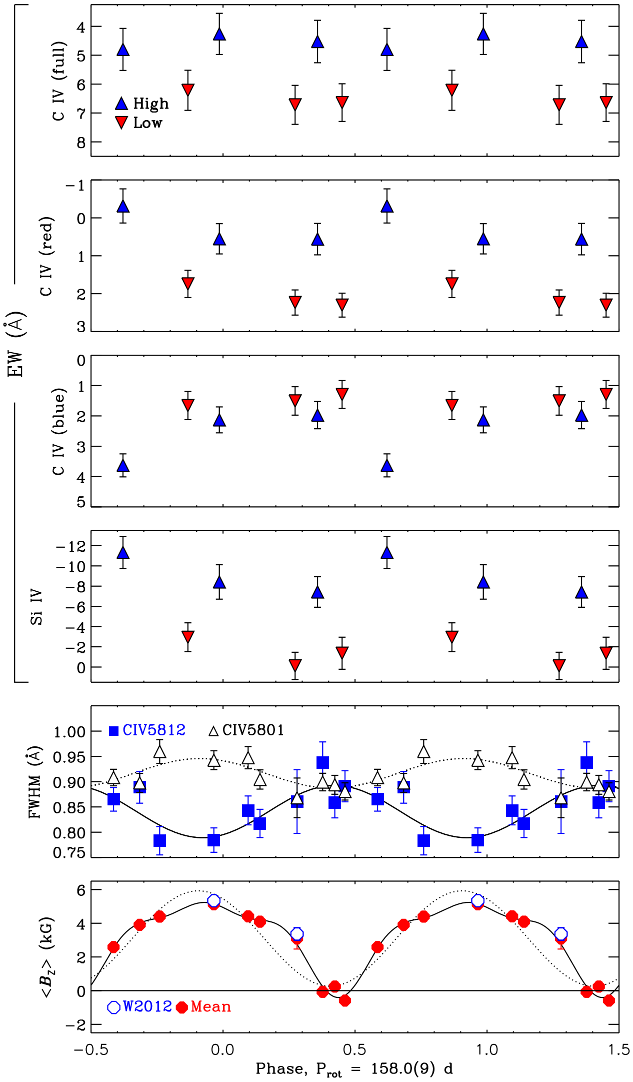

Figure 2. Top four panels: equivalent widths, folded with the rotation period, of (in order from the top) the blue side of the C IV profile, the low- and high-velocity portions of the blue side of the C IV doublet, and the Si IV doublet, within the ranges defined in Fig. 1. Observations at high- and low-state-like phases are indicated by upward-pointing blue and downward-pointing red triangles, respectively. We can see that all three low-state-like measurements agree within errors for each of the four wavelength ranges, while the high-state-like measurements have different values and are relatively consistent with each other (with the point at phase 0.621 exhibiting slightly more extreme behaviour). Fifth panel: full width at half-maximum (FWHM) of the C IV $\lambda 5801$ and $\lambda 5812$ lines, as a proxy to the magnetic modulus. Solid and dotted curves are harmonic fits. Bottom panel: weighted mean $\langle B_z \rangle$ measurements across all lines (including those yielded by the spectra used by Wade et al. 2012, in blue, which we reanalysed for uniformity – our results are consistent, within errors, with theirs). Solid and dotted curves show third- and first-order harmonic fits, respectively.

as two separate ranges within the blue side of the C IV doublet corresponding to high/low velocities. These ranges were chosen to best illustrate the interplay between emission and absorption effects, based on the phenomenology described above. The results of our measurements are shown in the top four panels of Fig. 2. We can see that for a given integration range, all three equivalent width measurements taken at low-state-like phases (represented by downward-pointing red triangles) are consistent with each other within the error bars. Similarly, the high-state-like measurements (represented by upward-pointing blue triangles) are also relatively consistent with each other, with the exception of the point at phase 0.621, especially for the high-velocity absorption on the blue side of the C IV doublet. They are also clearly distinct from the low-state-like measurements, except once again in the case of the high-velocity absorption in the C IV doublet, for which the difference between both sets of measurements is not significant within the errors, though systematic. Furthermore, the overall behaviour corresponds to what can be seen from the line profiles themselves and to the general phenomenological picture presented above, although the phasing cannot be explained in the context of a dipolar magnetic field (as also evidenced by the difference between these equivalent width curves and those of other magnetic O-type stars, such as HD 191612, thought to have a dipolar magnetic field; Marcolino et al. 2013). The Si IV doublet shows greatly enhanced emission at high-state-like phases, presumably due to dense confined material seen off the limb of the star. Meanwhile, the high-velocity absorption trough of the C IV doublet shows deeper absorption when the star is viewed in such a way that fast-flowing wind material along open field lines intersects the line of sight (high-state-like phases), and conversely the low-velocity absorption near line centre is enhanced when an accumulation of wind material confined near the surface occults the stellar disc (low-state-like phases). These combined effects lead to enhanced absorption at low-state-like phases in the full range of the absorption trough of the C IV doublet. Additional UV diagnostics also show a similar dichotomy, such as the ‘forest’ of photospheric Fe IV lines in the 1615–1630 Å range, which show enhanced absorption at low-state-like phases, as found by David-Uraz et al. (2019).

In principle, it appears as though these observations might provide some support for the hypothesis of a complex field (i.e. departing from a simple dipole), as investigated in greater detail below. We also attempt to develop further inferences on the global structure of the magnetosphere in Section 4.2.

3.2 Magnetic analysis

The optical spectra were continuum normalized and co-added (for spectra taken within a few days of each other, hence similar rotational phase), and then used to measure the disc-averaged line-of-sight magnetic field $\langle B_z \rangle$ (as defined by Mathys 1989) from a selection of spectral lines chosen to be strong, isolated, and relatively uncontaminated by wind emission. The laboratory wavelengths and Landé factors (given in Table A3, along with the measurements from each line) were obtained from a line list downloaded from the Vienna Atomic Line Database, version 3.0 (VALD3; Piskunov et al. 1995; Ryabchikova et al. 1997, 2015; Kupka et al. 1999, 2000) with an ‘extract stellar’ request formulated with NGC 1624−2’s stellar parameters ($T_{\rm eff} = 35$ kK, $\log g = 4.0$; Wade et al. 2012). The null field $\langle N_z \rangle$ was also obtained from the diagnostic N profile in the same fashion; $\langle N_z \rangle$ is consistent with 0 in all measurements. Integration ranges were determined using the test described by Neiner et al. (2012), i.e. progressively widening the integration range until $\langle B_z \rangle$ converges to a constant value, and selecting the integration range yielding the minimum error bar.

The bottom panel of Fig. 2 shows $\langle B_z \rangle$ folded with the 157.99 d rotation period (Wade et al. 2012). As can be seen in Fig. 2, where we show the weighted mean obtained from single-line measurements from co-added spectra, there is good agreement between the $\langle B_z \rangle$ measured here and the measurements reported by Wade et al. (2012, their table 6).

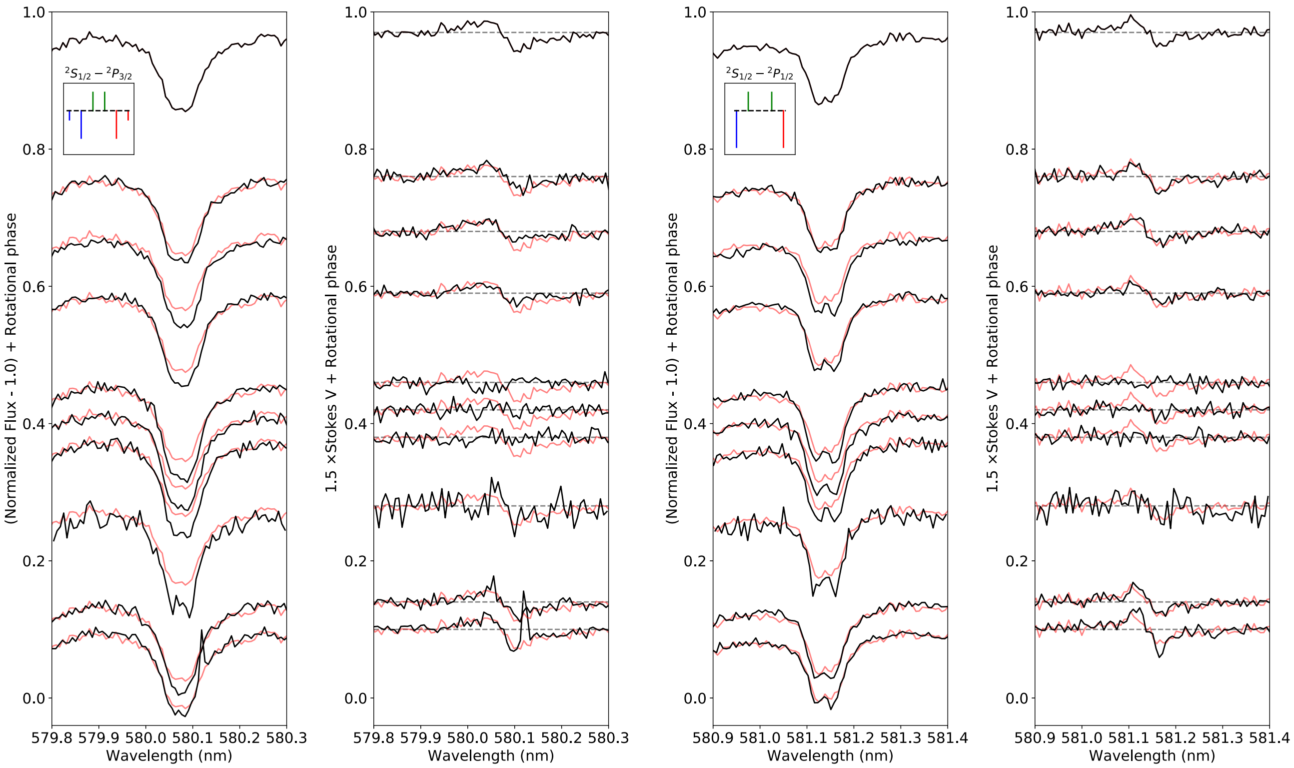

Figure 3. Spectropolarimetric data set with vertical offset according to the rotational phase, for the C IV λ5801 (left two panels) and C IV λ5812 (right two panels) lines. The spectra were binned (2-pixel bins) for display purposes. The Zeeman patterns (on the same horizontal and vertical scales) are shown in the insets. The spectrum of the observations closest to phase 0 is overlaid with each subsequent spectrum, in pale red, to highlight the variation with phase.

Measurements from individual lines are given in Table A3. Notably, there are few statistically significant differences in results from He lines, the C IV λ5801 line, or the O III λ5592 line. This suggests that wind contamination in these lines is indeed minimal (or at least, at a similarly low level). Exceptions are He I λ4713, and He II λ5412, which both yield lower amplitudes than other lines, likely due to wind contamination. The similarity of results across C, O, and most He lines furthermore confirms that Stokes V is not affected by the presence of chemical spots, which can lead to large discrepancies in $\langle B_z\rangle$ measurements obtained from different chemical species in cooler stars with Bp-type chemical peculiarities (e.g. Shultz et al. 2015, 2018; Yakunin et al. 2015). This is not surprising, as the strong winds of O-type stars are expected to render atomic diffusion inefficient in these stars by removing the outer layer where mass segregation occurs, inhibiting the formation of surface chemical spots (e.g. Michaud et al. 1987).

On the other hand, $\langle B_z\rangle$ measurements made using the C IV λ5812 line exhibit clear departures from the other lines. This is almost certainly a result of the high magnetic sensitivity of this line, which causes its shape to be broadened by the field and affects the measurements. Indeed, as pointed out by Wade et al. (2012), Zeeman splitting (which scales with the Landé factor of each line) is visible in the C IV λ5801 and λ5812 lines. Fig. 3 shows the profile variations over phase for both lines. The spectrum nearest to the high state (phase 0.97) is overlaid with each spectrum to highlight the phase variation. We notice that magnetic splitting is seen at all phases in the C IV λ5812 line.

The fifth panel of Fig. 2 shows the full width at half-maximum (FWHM) of the C IV λ5801 and λ5812 lines folded with the same rotational period (157.99 d) used for the bottom panel, as a proxy of the magnetic modulus. A direct measurement of the modulus, by fitting synthetic profiles to the observed lines, is made challenging by the large degeneracies between the magnetic, thermal and turbulent broadening mechanisms, since only a few km s^{-1} of extra turbulent broadening, for instance, leads to large differences in the inferred modulus. Nevertheless, the FWHM of these C IV lines appears to exhibit rotational modulation: the reduced χ^2 of a harmonic fit to the C IV λ5812 line is 1.3, as compared to 2.9 for the null hypothesis of no variation about the mean value, and its FWHM peaks at around phase 0.5. While the null hypothesis cannot quite be formally ruled out (at a 99 per cent confidence threshold), this result still strongly suggests that rotational modulation is present, a result that could be better confirmed with higher signal-to-noise ratio (S/N) observations. By contrast, the less magnetically sensitive C IV λ5801 line[3] shows an anticorrelated variation, likely due to the fact that its wings and width appear to change only minimally, while its depth varies, leading to a smaller FWHM when the line is deeper (e.g. around phase 0.5, as can be seen in Fig. 3). Since there is no reason to expect that turbulent or thermal broadening varies horizontally across the stellar surface, the variation in the FWHM of the C IV λ5812 line is most likely due to variation in the magnetic modulus.

Curiously, the FWHM of the C IV λ5812 line – and therefore also the magnetic modulus, assuming that all variations in the FWHM

---

[3] Though the difference between the effective Landé factor of this line (1.167) and that of the C IV λ5812 line (1.333) is not that large, the Zeeman pattern of this line is also more complex (six components) and less well resolved, probably leading to a more marginal variation of the magnetic broadening. Detailed modelling of the line profile would be required to include this line in the study of the magnetic field modulus.

result from variations in the modulus – is at a maximum near phase 0.5, at which phase $\langle B_z \rangle$ is consistent with 0. This behaviour is not expected for a dipolar magnetic field, as the magnetic modulus at the equator of a dipole should instead be at its minimum, but is commonly seen in Ap stars, for which the measured field modulus variations can be reproduced by adding a quadrupolar component to the global field topology (e.g. Landstreet & Mathys 2000). Further indication that the field is probably not purely dipolar is given by the harmonic fit to the mean $\langle B_z \rangle$ measurements (calculated from all lines except the discrepant C IV λ5812 line). A first-order fit, as would be appropriate to a dipolar field, yields a reduced χ^2 of 10.8, as compared to 4.5 when $\langle B_z \rangle$ is fit with three harmonics (Fig. 2, bottom panel).

4 DISCUSSION AND CONCLUSIONS

4.1 Rotational period

The first thing to rule out as a means of interpreting the variation of the UV spectrum is the possibility that the rotational period, calculated using equivalent width measurements of a few lines and line ratios by Wade et al. (2012), is wrong. While they already provide compelling arguments as to why other periods are not suitable to reproduce the variations of these lines, we further investigate whether a different rotational period would help make sense of the UV observations presented above.

If the current rotational period is wrong, while spectra with similar line morphologies might not have been obtained at exactly the same rotational phase, within a dipolar field framework, one would imagine that they were obtained at relatively close phases (within a difference of up to ∼0.2 cycles). In particular, the spectra obtained at phases 0.27 and 0.87 (with respect to the published ephemerides) are nearly identical in character, yet they were obtained only ∼60 d apart. This could suggest either that the period is significantly longer (or shorter) than the published value.

First, assuming for instance that the equivalent widths of the aforementioned lines undergo a double-wave variation over a single rotational cycle, one might surmise that the ‘real’ period is in fact 315.98 d, or twice the previously inferred value. Such a period would encompass all of our new UV observations, and while the UV line profiles phased with this longer period appear to vary in a more coherent manner, they do so in a single-wave pattern, which is inconsistent with the global picture derived from other observational diagnostics, which would then show a double-wave variation in this assumed scenario.

On the other hand, if we consider the possibility of the period being shorter (perhaps by a factor of 2 or 3, given the UV observations), we encounter further complications. Not only are significantly shorter periods ruled out by the equivalent width analysis performed by Wade et al. (2012), down to 60 d, but they are also difficult to reconcile with the profiles of photospheric lines in the optical spectra of NGC 1624−2. Wade et al. (2012) place an upper limit on $v\sin i$ of 15 km s^{-1}, based on the modelling of the C IV λ5801 line, assuming macroturbulent broadening, but without magnetic broadening. Conversely, when they model this line (which is quite magnetically sensitive due to its high Landé factor) using Zeeman broadening, they find their best fit to be consistent with all of the broadening being accounted for by the Zeeman effect (as discussed above), or essentially no rotational broadening. Based on their estimated values for the stellar radius ($R_* = 10\ \mathrm{R}_\odot$) and their measured rotation period, they find an upper limit on the equatorial rotational velocity of ∼3.2 km s^{-1}. Increasing that value by a factor of 2 or more requires us to adopt a fairly low value of the inclination angle i, which does not appear to be consistent with the large variations seen in the UV. The magnetic measurements presented in Figs 2 and 3 also phase well with the published period, and rule out a period that is significantly different from that value, or possibly its double (in the case of a double-wave variation of the longitudinal field).

While we cannot, within the scope of this paper, constrain a firm lower limit on the inclination based on UV variations alone, further modelling of the surface magnetic field, including modelling of the photospheric line profiles, is in progress and should conclusively resolve this issue. In the meantime, however, we infer that the previously derived rotational period is probably correct, or sufficiently close to the *real* value that it does not affect the interpretation that similar line morphologies are observed at three separate rotational phases.

4.2 Magnetospheric structure and surface magnetic geometry

The most obvious hypothesis to attempt to explain the puzzling behaviour of the UV resonance lines of NGC 1624−2 involves a complex magnetospheric structure, with significant departures from what would be expected in the case of a purely dipolar surface magnetic field interacting with the stellar wind. Our preliminary magnetic analysis shows that the surface magnetic field of NGC 1624−2 is likely better modelled using a more complex geometry, though the determination of the detailed magnetic geometry is outside the scope of this paper. While this explanation appears satisfying from the point of view of these observations, it also appears at odds with the behaviour of optical lines (Wade et al. 2012), in particular He II λ4686 (their fig. 5), which despite certain gaps in phase coverage, seems to behave in a fairly monotonic way between high state (phase 0.0) and low state (phase 0.5), and vice versa. This behaviour is more in line with what is observed in the optical lines of other magnetic O stars, whose fields are inferred to be dipolar, such as HD 191612 (Marcolino et al. 2013).

One possibility is that the explanation could reside not necessarily in the complexity of the field responsible for the formation of the magnetosphere, but instead arise as a consequence of dynamic flows within the magnetosphere, predicted in MHD simulations to occur (e.g. ud-Doula & Owocki 2002). It could be that some observational diagnostics – especially those formed further away from the stellar surface, such as the UV resonance lines – are more sensitive to these flows than others, which are dominated by averaging effects. However, while this could explain some discrepancies at low velocities, it is difficult to produce high-velocity blueshifted absorption (as observed in the C IV λλ1548, 1550 doublet) using these dynamic flows. In fact, investigations of different implementations of the ADM model using material either flowing up or down closed field loops (mimicking in a way the aforementioned flows) do not lead to any variations in the line profile past a velocity of about 70 per cent of the inferred terminal velocity (Hennicker et al. 2018). The increased depth of the C IV doublet at high velocity at rotational phases 0.274, 0.621, and 0.986 suggests that we are looking down open field lines, something that can only occur, as far as we can tell, if the field is topologically complex (given that this line is understood to form throughout most of the wind, therefore probing its full structure).

While the detailed geometry of the surface magnetic field cannot be inferred from the effect that it has on the magnetospheric structure and hence on the variation of UV resonance line profiles, better spectropolarimetric phase coverage and surface mapping techniques such as Zeeman–Doppler Imaging (ZDI; Semel 1989; Piskunov & Kochukhov 2002) have the potential of shedding light on NGC

1624−2's potentially complex magnetic field. This topic will be addressed in more detail in a forthcoming publication.

4.3 Magnetic field origin and evolution

A photometric study of the NGC 1624 cluster has yielded an upper limit on the main-sequence turnoff age of 4 Myr (Lim et al. 2015). A better characterization of this cluster (and in particular of its massive star population by means of quantitative spectroscopy) would prove useful to get a more precise age and better constrain the evolutionary status of NGC 1624−2.

This question is of particular relevance in the context of the origin of magnetic fields in massive stars and their evolution. It has been suggested that their fields might decay over time (e.g. Landstreet et al. 2007, 2008; Fossati et al. 2016), and that the decay rate increases with higher mass, from near-flux conservation in A stars (Sikora et al. 2019) to stronger flux decay in OB stars (Shultz et al. 2019). Assuming Ohmic dissipation to be the mechanism by which these fields decay, higher order multipolar components are expected to decay fastest (e.g. Charbonneau 2013, and references therein; there is also tentative evidence that complex fields decay faster than simple dipolar fields in OB stars, Shultz et al. 2019). Therefore, a strong, complex field might be consistent with the Ohmic dissipation scenario (and indicative of a young magnetic star, if its field is fossil in origin), and a more detailed characterization of the field topology of magnetic high-mass stars might prove crucial to reveal the phenomena influencing the evolution of magnetism in these stars.

Alternatively, stellar mergers have been proposed as a viable channel for the formation of magnetic fields in massive stars (Ferrario et al. 2009; Schneider et al. 2016, 2019, 2020). While merger products are expected to potentially exhibit large surface enhancements of hydrogen-burning products such as helium and nitrogen (Glebbeek et al. 2013), NGC 1624−2 is believed to show at most only a moderate nitrogen surface enrichment (Wade et al. 2012), though the precise abundance is difficult to determine due partly to the uncertainties on the strength of the magnetic field and the effective temperature. A more thorough evaluation of the merger hypothesis in the specific case of NGC 1624−2 can only be conducted once its environment is better characterized, including especially abundance analyses of other massive stars in the cluster.

4.4 Conclusions

The line profile variations observed in *HST*/COS spectra of NGC 1624−2 over six separate rotational phases do not correspond to the expected phenomenology – as established by observations of other magnetic O-type stars, or modelled using MHD simulations or the ADM prescription – which accounts for a magnetosphere formed by the interaction of a strong stellar wind and a global dipolar field. Instead, the observed line profiles appear to exhibit one of two morphologies, previously understood – within the aforementioned scenario – to correspond to either a magnetic pole-on or magnetic equator-on view of the magnetosphere. Furthermore, a magnetic analysis using spectropolarimetric observations shows that the diagnostics of NGC 1624−2's surface magnetic field cannot be well reproduced using a purely dipolar geometry, assuming that the FWHM of the C IV λ5812 line acts as an appropriate proxy for the field modulus. Having exhausted more mundane explanations such as an error in the determination of the rotation period (such that our rotational phase determinations are sufficiently wrong to change the overall phenomenological picture) and short-term stochastic variations, we conclude that the magnetosphere of NGC 1624−2 is likely more structured than previously assumed, and that its surface magnetic field might depart from a dipolar geometry. While challenges remain in trying to reconcile such a scenario with other diagnostics (e.g. the smooth variations with phase of the equivalent widths of optical emission lines), only further modelling accounting for the detailed geometry of the field and the resulting distribution of plasma within the magnetosphere will allow us to self-consistently reproduce diagnostics ranging across multiple wavelength bands. Nevertheless, the perspective of the strongest known magnetic field on an O-star also being topologically complex provides us with crucial information regarding the formation and evolution of such fields on massive stars and further emphasizes the singular importance of this archetypal object.

ACKNOWLEDGEMENTS

Some of the data presented in this paper were obtained from the Mikulski Archive for Space Telescopes (MAST). This work has made use of the VALD data base, operated at Uppsala University, the Institute of Astronomy RAS in Moscow, and the University of Vienna. AD-U and VP acknowledge support for this work through program HST-GO-15066.001-A that was provided by NASA through a grant from the Space Telescope Science Institute, which is operated by the Association of Universities for Research in Astronomy, Inc., under NASA contract NAS 5-26555.

AD-U and GAW gratefully acknowledge the support of the Natural Sciences and Engineering Research Council of Canada (NSERC). VP acknowledges support from the University of Delaware Research Foundation. This study is based upon work supported by the National Science Foundation under grant no. 1747658. MES acknowledges support from the Annie Jump Cannon Fellowship, supported by the University of Delaware and endowed by the Mount Cuba Astronomical Observatory. CE acknowledges graduate assistant salary support from the Bartol Research Institute in the Department of Physics and Astronomy, University of Delaware, as well as support from program HST-GO-13629.002-A that was provided by NASA through a grant from the Space Telescope Science Institute.

Finally, the authors also thank D. H. Cohen, as well as the anonymous referee of this paper, for useful discussions and feedback that contributed to improve this paper.

This study is based on observations made at the Canada–France–Hawaii Telescope (CFHT).

DATA AVAILABILITY

The ultraviolet spectroscopic data underlying this paper are available in the Mikulski Archive for Space Telescopes (MAST) at https://archive.stsci.edu/, and are uniquely identified with the observation identifiers (ObsID) listed in Table A1. The optical spectropolarimetric data underlying this paper are available in the Canadian Astronomy Data Center (CADC) archive at https://www.cadc-ccda.hia-iha.nrc-cnrc.gc.ca/en/ and the PolarBase data base (Donati et al. 1997; Petit et al. 2014) available at http://polarbase.irap.omp.eu/, and are uniquely identified with the ObsIDs listed in Table A2.

REFERENCES

Babel J., Montmerle T., 1997, ApJ, 485, L29

Blazère A., Neiner C., Tkachenko A., Bouret J.-C., Rivinius T., 2015, A&A, 582, A110

Bouret J. C., Lanz T., Hillier D. J., Heap S. R., Hubeny I., Lennon D. J., Smith L. J., Evans C. J., 2003, ApJ, 595, 1182

Castor J. I., Abbott D. C., Klein R. I., 1975, ApJ, 195, 157

Charbonneau P., 2013, Saas-Fee Advanced Courses Vol. 39, Solar and Stellar Dynamos. Springer-Verlag, Berlin

Chu Y.-H., 2003, in van der Hucht K., Herrero A., Esteban C., eds, Proc. IAU Symp. 212, A Massive Star Odyssey: From Main Sequence to Supernova. Astron. Soc. Pac., San Francisco, p. 585

David-Uraz A., Petit V., MacInnis R., Erba C., Owocki S. P., Fullerton A. W., Walborn N. R., Cohen D. H., 2017, in Eldridge J. J., Bray J. C., McClelland L. A. S., Xiao L., eds, Proc. IAU Symp. Vol. 329, The Lives and Death-Throes of Massive Stars. Cambridge Univ. Press, Cambridge, p. 394

David-Uraz A. et al., 2019, MNRAS, 483, 2814

Donati J.-F., Semel M., Carter B. D., Rees D. E., Collier Cameron A., 1997, MNRAS, 291, 658

Donati J. F., Catala C., Landstreet J. D., Petit P., 2006, in Casini R., Lites B. W., eds, ASP Conf. Ser. Vol. 358, Solar Polarization 4. Astron. Soc. Pac., San Francisco, p. 362

Erba C., Petit V., David-Uraz A., Fullerton A., 2020, in Wade G., Alecian E., Bohlender D., Sigut A., eds, Proc. Polish Astron. Soc. Vol. 11, Stellar Magnetism: A Workshop in Honour of the Career and Contributions of John D. Landstreet. Polish Astron. Soc., Warsaw, Poland, p. 74

Ferrario L., Pringle J. E., Tout C. A., Wickramasinghe D. T., 2009, MNRAS, 400, L71

Ferrario L., Wickramasinghe D., 2008, MNRAS, 389, L66

Fossati L. et al., 2016, A&A, 592, A84

Georgy C., Meynet G., Ekström S., Wade G. A., Petit V., Keszthelyi Z., Hirschi R., 2017, A&A, 599, L5

Glebbeek E., Gaburov E., Portegies Zwart S., Pols O. R., 2013, MNRAS, 434, 3497

Groh J. H., Farrell E. J., Meynet G., Smith N., Murphy L., Allan A. P., Georgy C., Ekstroem S., 2020, ApJ, 900, 98

Grunhut J. H. et al., 2013, MNRAS, 428, 1686

Grunhut J. H. et al., 2017, MNRAS, 465, 2432

Hennicker L., Puls J., Kee N. D., Sundqvist J. O., 2018, A&A, 616, A140

Keszthelyi Z., Meynet G., Georgy C., Wade G. A., Petit V., David-Uraz A., 2019, MNRAS, 485, 5843

Keszthelyi Z. et al., 2020, MNRAS, 493, 518

Kupka F. G., Piskunov N., Ryabchikova T. A., Stempels H. C., Weiss W. W., 1999, A&AS, 138, 119

Kupka F. G., Ryabchikova T. A., Piskunov N. E., Stempels H. C., Weiss W. W., 2000, Balt. Astron., 9, 590

Lamers H. J. G. L. M., Snow T. P., Lindholm D. M., 1995, ApJ, 455, 269

Landi degl'Innocenti E., Landolfi M., 2004, Polarization in Spectral Lines. Kluwer, Dordrecht

Landstreet J. D., Bagnulo S., Andretta V., Fossati L., Mason E., Silaj J., Wade G. A., 2007, A&A, 470, 685

Landstreet J. D., Borra E. F., 1978, ApJ, 224, L5

Landstreet J. D., Mathys G., 2000, A&A, 359, 213

Landstreet J. D. et al., 2008, A&A, 481, 465

Lim B., Sung H., Bessell M. S., Kim J. S., Hur H., Park B.-G., 2015, AJ, 149, 127

MacInnis R., 2016, Master's thesis, Department of Physics and Space Sciences, Florida Institute of Technology, Melbourne, FL

Marcolino W. L. F., Bouret J.-C., Sundqvist J. O., Walborn N. R., Fullerton A. W., Howarth I. D., Wade G. A., ud-Doula A., 2013, MNRAS, 431, 2253

Martioli E., Teeple D., Manset N., 2011, in Gajadhar S. et al., eds, Telescopes from Afar. p. 63. Available at: http://tfa.cfht.hawaii.edu

Mathys G., 1989, Fundamentals Cosmic Phys., 13, 143

Meynet G., Eggenberger P., Maeder A., 2011, A&A, 525, L11

Michaud G., Dupuis J., Fontaine G., Montmerle T., 1987, ApJ, 322, 302

Morel T. et al., 2015, in Meynet G., Georgy C., Groh J., Stee P., eds, Proc. IAU Symp. Vol. 307, New Windows on Massive Stars: Asteroseismology, Interferometry, and Spectropolarimetry. Cambridge Univ. Press, Cambridge, p. 342

Munoz M. S., Wade G. A., Nazé Y., Puls J., Bagnulo S., Szymański M. K., 2020, MNRAS, 492, 1199

Nazé Y., Petit V., Rinbrand M., Cohen D., Owocki S., ud-Doula A., Wade G. A., 2014, ApJS, 215, 10

Nazé Y., Sundqvist J. O., Fullerton A. W., ud-Doula A., Wade G. A., Rauw G., Walborn N. R., 2015, MNRAS, 452, 2641

Nazé Y., ud-Doula A., Spano M., Rauw G., De Becker M., Walborn N. R., 2010, A&A, 520, A59

Neiner C., Alecian E., Briquet M., Floquet M., Frémat Y., Martayan C., Thizy O., Mimes Collaboration, 2012, A&A, 537, A148

Owocki S. P., ud-Doula A., 2004, ApJ, 600, 1004

Owocki S. P., ud-Doula A., Sundqvist J. O., Petit V., Cohen D. H., Townsend R. H. D., 2016, MNRAS, 462, 3830

Petit P., Louge T., Théado S., Paletou F., Manset N., Morin J., Marsden S. C., Jeffers S. V., 2014, PASP, 126, 469

Petit V. et al., 2013, MNRAS, 429, 398

Petit V. et al., 2015, MNRAS, 453, 3288

Petit V. et al., 2017, MNRAS, 466, 1052

Petit V. et al., 2019, MNRAS, 489, 5669

Piskunov N., Kochukhov O., 2002, A&A, 381, 736

Piskunov N. E., Kupka F., Ryabchikova T. A., Weiss W. W., Jeffery C. S., 1995, A&AS, 112, 525

Ryabchikova T., Piskunov N., Kurucz R. L., Stempels H. C., Heiter U., Pakhomov Y., Barklem P. S., 2015, Phys. Scr., 90, 054005

Ryabchikova T. A., Piskunov N. E., Kupka F., Weiss W. W., 1997, Balt. Astron., 6, 244

Schneider F. R. N., Ohlmann S. T., Podsiadlowski P., Röpke F. K., Balbus S. A., Pakmor R., 2020, MNRAS, 495, 2796

Schneider F. R. N., Ohlmann S. T., Podsiadlowski P., Röpke F. K., Balbus S. A., Pakmor R., Springel V., 2019, Nature, 574, 211

Schneider F. R. N., Podsiadlowski P., Langer N., Castro N., Fossati L., 2016, MNRAS, 457, 2355

Semel M., 1989, A&A, 225, 456

Shore S. N., Brown D. N., 1990, ApJ, 365, 665

Shultz M., Wade G. A., 2017, MNRAS, 468, 3985

Shultz M. E. et al., 2018, MNRAS, 475, 5144

Shultz M. E. et al., 2019, MNRAS, 490, 274

Shultz M. et al., 2015, MNRAS, 449, 3945

Sikora J., Wade G. A., Power J., Neiner C., 2019, MNRAS, 483, 3127

Stibbs D. W. N., 1950, MNRAS, 110, 395

ud-Doula A., Owocki S. P., 2002, ApJ, 576, 413

ud-Doula A., Owocki S. P., Townsend R. H. D., 2008, MNRAS, 385, 97

ud-Doula A., Owocki S. P., Townsend R. H. D., 2009, MNRAS, 392, 1022

Wade G. A. et al., 2012, MNRAS, 425, 1278

Wade G. A. et al., 2016, MNRAS, 456, 2

Walborn N. R., 1972, AJ, 77, 312

Walborn N. R., Sota A., Maíz Apellániz J., Alfaro E. J., Morrell N. I., Barbá R. H., Arias J. I., Gamen R. C., 2010, ApJ, 711, L143

Weber E. J., Davis L., Jr, 1967, ApJ, 148, 217

Yakunin I. et al., 2015, MNRAS, 447, 1418

APPENDIX: JOURNAL OF OBSERVATIONS

In this section, we list the *HST*, CFHT, and TBL observations used in the context of this study, as well as the longitudinal magnetic field measurements performed using the latter two (Tables A1–A3).

Table A1. Journal of COS observations.

ObsID	Program ID	Grating	λ_c[a] (Å)	S/N[b]	UT (start)	Exp. time (s)	MJD(mid)	ϕ[c]
lcl601010	13734	G130M	1291	10.6	2015-02-17T06:16:42	848	57070.2685	0.986
lcl601020	13734	G130M	1327	10.1	2015-02-17T06:39:53	844	57070.2846	0.986
lcl601030	13734	G160M	1577	16.1	2015-02-17T07:40:05	1084	57070.3279	0.986
lcl601040	13734	G160M	1623	16.0	2015-02-17T08:07:48	1080	57070.3472	0.986
lcl602010	13734	G130M	1291	10.2	2015-10-06T16:20:53	848	57301.6881	0.451
lcl602020	13734	G130M	1327	9.9	2015-10-06T16:44:04	844	57301.7042	0.451
lcl602030	13734	G160M	1577	15.6	2015-10-06T17:07:58	1084	57301.7309	0.451
lcl602040	13734	G160M	1623	15.6	2015-10-06T18:00:30	1080	57301.7588	0.452
ldmu04010	15066	G130M	1222	10.5	2018-02-08T09:59:05	940	58157.4233	0.867
ldmu04020	15066	G130M	1291	12.0	2018-02-08T10:23:13	940	58157.4390	0.868
ldmu04030	15066	G160M	1577	15.7	2018-02-08T11:25:11	1080	58157.4842	0.868
ldmu04040	15066	G160M	1623	15.6	2018-02-08T11:52:50	1080	58157.5033	0.868
ldmu01010	15066	G130M	1222	10.4	2018-04-13T13:44:46	940	58221.5927	0.274
ldmu01020	15066	G130M	1291	11.9	2018-04-13T14:45:31	940	58221.6212	0.274
ldmu01030	15066	G160M	1577	15.4	2018-04-13T15:20:10	1080	58221.6605	0.274
ldmu01040	15066	G160M	1623	15.6	2018-04-13T16:25:40	1080	58221.6986	0.274
ldmu02010	15066	G130M	1222	10.4	2018-10-01T21:47:01	940	58392.9149	0.358
ldmu02020	15066	G130M	1291	12.0	2018-10-01T23:00:25	940	58392.9648	0.358
ldmu02030	15066	G160M	1577	15.6	2018-10-01T23:22:25	1080	58393.0032	0.359
ldmu02040	15066	G160M	1623	15.8	2018-10-02T00:50:19	1080	58393.0432	0.359
ldmu03010	15066	G130M	1222	10.6	2018-11-12T11:23:02	940	58434.4816	0.621
ldmu03020	15066	G130M	1291	12.0	2018-11-12T12:30:57	940	58434.5277	0.622
ldmu03030	15066	G160M	1577	15.9	2018-11-12T12:52:57	1080	58434.5452	0.622
ldmu03040	15066	G160M	1623	15.8	2018-11-12T14:06:15	1080	58434.5959	0.622

Notes. [a]Central wavelength of the grating setting.
[b]Computed per 9-pixel resolution element between 1350 and 1355 Å (G130M) or 1490 and 1495 Å (G160M).
[c]Phase of MJD(mid) according to the ephemeris of Wade et al. (2012).

Table A2. Observations of NGC 1624−2 from ESPaDOnS at CFHT and NARVAL at TBL (in italic). In this table HJD is the Heliocentric Julian Date, and JD0 is the arbitrary Julian Date chosen as the starting point to record the rotations of NGC 1624−2. The rotation numbers and phases are based on JD0 and NGC 1624−2's well-defined rotation period of 157.99 d.

Date	ObsID	HJD – 245 0000	Rotations since JD0	Phase	Mean phase	Mean $\langle B_z \rangle$ (kG)	Mean $\langle N_z \rangle$ (kG)
2012-02-01	1522987p	5958.7154	−1	0.948 ± 0.06	0.97 ± 0.06	5.10 ± 0.22	0.13 ± 0.22
2012-02-02	1523106p	5959.7155	−1	0.954 ± 0.06			
2012-02-03	1523413p	5960.7132	−1	0.960 ± 0.06			
2012-02-04	1523605p	5961.7128	−1	0.966 ± 0.06			
2012-02-09	1524145p	5966.7204	−1	0.998 ± 0.06			
2012-03-24	*119496o*	*6011.3316*	*0*	*0.281 ± 0.06*	*0.28 ± 0.06*	*3.1 ± 0.6*	*0.1 ± 0.6*
2012-09-27	1573465p	6197.9445	1	0.462 ± 0.07	0.46 ± 0.07	−0.49 ± 0.21	−0.38 ± 0.21
2012-09-27	1573469p	6198.0090	1	0.462 ± 0.07			
2013-08-27	1650338p	6532.1192	3	0.577 ± 0.09	0.59 ± 0.09	2.67 ± 0.18	0.23 ± 0.19
2013-08-29	1650656p	6534.0561	3	0.589 ± 0.09			
2013-08-29	1650660p	6534.1180	3	0.590 ± 0.09			
2013-09-13	1653352p	6549.0333	3	0.684 ± 0.09	0.68 ± 0.09	3.75 ± 0.23	−0.00 ± 0.23
2013-09-13	1653356p	6549.0961	3	0.684 ± 0.09			
2013-09-25	1656332p	6561.0236	3	0.760 ± 0.09	0.76 ± 0.09	4.46 ± 0.28	0.53 ± 0.28
2013-09-25	1656336p	6561.0859	3	0.760 ± 0.09			
2013-11-17	1669969p	6613.9090	4	0.095 ± 0.09	0.10 ± 0.09	4.24 ± 0.24	−0.14 ± 0.24
2013-11-17	1669981p	6614.0410	4	0.095 ± 0.09			
2013-11-24	1671235p	6621.0356	4	0.140 ± 0.09	0.14 ± 0.09	3.97 ± 0.27	0.50 ± 0.27
2013-11-24	1671239p	6621.0978	4	0.140 ± 0.09			
2014-01-08	1682621p	6665.8216	4	0.423 ± 0.09	0.42 ± 0.09	0.37 ± 0.28	−0.32 ± 0.28
2014-01-08	1682625p	6665.8835	4	0.424 ± 0.09			
2015-09-24	1834775p	7290.0362	8	0.374 ± 0.11	0.38 ± 0.11	−0.43 ± 0.27	−0.25 ± 0.27
2015-09-25	1834930p	7291.0543	8	0.381 ± 0.11			

Table A3. $\langle B_z \rangle$ measurements from individual lines, in kG. The second row under each line of the table heading gives the Landé factor of each line, as found in the output of the VALD data base, or computed from LS coupling. In the case of multiplets, the highest value among the components of the line complex is shown.

HJD –	He I 4471	He I 4713	He I 4922	He I 5016	He I 7281	He II 5412	C IV 5801	C IV 5812	O III 5592
245 0000	1.333	1.750	1.000	1.200	1.000	1.200	1.167	1.333	1.000
5961.5156	6.7 ± 1.7	3.3 ± 0.5	6.0 ± 0.6	3.7 ± 0.4	4.8 ± 0.4	4.0 ± 0.5	6.2 ± 0.5	4.0 ± 0.6	6.2 ± 0.9
6011.3316	1.0 ± 3.1	2.9 ± 1.9	2.9 ± 1.9	2.1 ± 1.1	2.8 ± 1.1	4.8 ± 1.6	3.0 ± 1.3	3.0 ± 1.8	2.3 ± 2.9
6197.9766	− 0.1 ± 1.3	− 0.0 ± 0.5	− 0.6 ± 0.7	− 0.2 ± 0.3	− 1.0 ± 0.4	− 0.7 ± 0.7	− 0.7 ± 0.6	0.0 ± 0.5	− 0.3 ± 1.0
6533.4312	1.1 ± 1.3	1.5 ± 0.6	1.6 ± 0.7	2.1 ± 0.4	3.4 ± 0.4	2.0 ± 0.5	2.9 ± 0.4	2.0 ± 0.4	2.5 ± 0.9
6549.0645	4.4 ± 1.6	1.6 ± 0.7	3.0 ± 0.9	2.9 ± 0.3	4.1 ± 0.5	3.6 ± 0.6	4.7 ± 0.5	3.8 ± 0.6	3.0 ± 0.8
6561.0547	7.4 ± 2.2	2.3 ± 0.7	4.5 ± 1.0	3.6 ± 0.5	5.3 ± 0.5	3.7 ± 0.8	4.6 ± 0.7	2.9 ± 0.6	4.1 ± 1.0
6613.9751	0.2 ± 1.8	2.6 ± 0.6	3.4 ± 0.7	3.2 ± 0.3	5.3 ± 0.4	4.5 ± 0.8	4.1 ± 0.8	4.3 ± 0.6	4.6 ± 1.4
6621.0664	1.2 ± 1.4	2.0 ± 0.8	5.2 ± 0.8	3.1 ± 0.4	5.5 ± 0.6	3.8 ± 0.7	3.0 ± 0.8	3.3 ± 0.5	5.4 ± 1.0
6665.8525	1.1 ± 1.8	0.2 ± 0.8	− 0.2 ± 0.9	0.8 ± 0.6	0.9 ± 0.5	− 0.3 ± 0.7	− 0.4 ± 0.7	0.9 ± 0.6	− 1.8 ± 1.2
7290.5449	1.6 ± 2.0	− 0.9 ± 0.6	− 1.1 ± 1.0	− 0.4 ± 0.4	0.2 ± 0.5	0.9 ± 0.9	− 1.9 ± 0.7	0.4 ± 0.6	0.5 ± 1.1

This paper has been typeset from a TEX/LATEX file prepared by the author.